The formation, structure and physical properties of $M_2Pd_{14+x}B_{5-y}$ compounds, with M = La, Ce, Pr, Nd, Sm, Eu, Gd, Lu and Th

2009 J. Phys.: Condens. Matter 21 305401

(http://iopscience.iop.org/0953-8984/21/30/305401)

J. Phys.: Condens. Matter **21** (2009) 305401 (12pp) doi:10.1088/0953-8984/21/30/305401

The formation, structure and physical properties of $M_2Pd_{14+x}B_{5-y}$ compounds, with M = La, Ce, Pr, Nd, Sm, Eu, Gd, Lu and Th

E Royanian[1,2,5], E Bauer[1], H Kaldarar[1], A Galatanu[1], R T Khan[1], G Hilscher[1], H Michor[1], M Reissner[1], P Rogl[2], O Sologub[3], G Giester[4] and A P Gonçalves[3]

[1] Institute of Solid State Physics, Vienna University of Technology, A-1040 Wien, Austria
[2] Institute of Physical Chemistry, University of Vienna, A-1090 Wien, Austria
[3] Departamento de Quimica, Instituto Tecnologico e Nuclear, P-2686-953 Sacavém, Portugal
[4] Institute of Mineralogy and Crystallography, University of Vienna, Althanstrasse 14, A-1090 Wien, Austria

E-mail: royanian@ifp.tuwien.ac.at

Received 19 February 2009, in final form 5 June 2009
Published 6 July 2009
Online at stacks.iop.org/JPhysCM/21/305401

Abstract

Novel ternary compounds, $M_2Pd_{14+x}B_{5-y}$ (M = La, Ce, Pr, Nd, Sm, Eu, Gd, Lu, Th; $x \sim 0.9$, $y \sim 0.1$), have been synthesized by arc melting. The crystal structures of $Nd_2Pd_{14+x}B_{5-y}$ and $Th_2Pd_{14+x}B_{5-y}$ were determined from x-ray single-crystal data and both are closely related to the structure type of $Sc_4Ni_{29}B_{10}$. All compounds were characterized by Rietveld analyses and found to be isotypic with the $Nd_2Pd_{14+x}B_{5-y}$ type. Measurements of the temperature dependent susceptibility and specific heat as well as the temperature and field dependent resistivity were employed to derive basic information on bulk properties of these compounds. The electrical resistivity of $M_2Pd_{14+x}B_{5-y}$, in general, is characterized by small RRR (residual resistance ratio) values originating from defects inherent to the crystal structure. Whereas the compounds based on Ce, Nd, Sm and Gd exhibit magnetic order, those based on Pr and Eu seem to be non-magnetic, at least down to 400 mK. While the non-magnetic ground state of the Pr based compound is a consequence of crystalline electric field effects in the context of the non-Kramers ion Pr, the lack of magnetic order in the case of the Eu based compound results from an intermediate valence state of the Eu ion.

(Some figures in this article are in colour only in the electronic version)

1. Introduction

The recent discovery of $CePt_3Si$ ($CePt_3B$ type) as the first heavy fermion superconductor without a center of symmetry [1–4] has triggered widespread research activities to search for novel superconducting states in related ternary or quaternary alloy systems [5, 6].

To gain more insight into the general physical behavior in rare earth–noble metal–non-metal systems, our studies were extended to rare earth palladium boride ternaries. In the course of the present study, it turned out that besides the well known perovskite phases $REPd_3B_{1-x}$ [7–9] (RE is one of the light rare earth elements) novel and hitherto unknown compounds were found to exist near the composition $REPd_7B_{2.5}$ for all light rare earth elements from La to Gd. Furthermore the investigation was extended to include the actinoid elements Th and U. The present paper aims at a detailed investigation and evaluation of these compounds in order to characterize their crystal structure and thermodynamic, electric and magnetic behavior, and elucidate ground states and phase transitions appearing in this series.

[5] Author to whom any correspondence should be addressed.

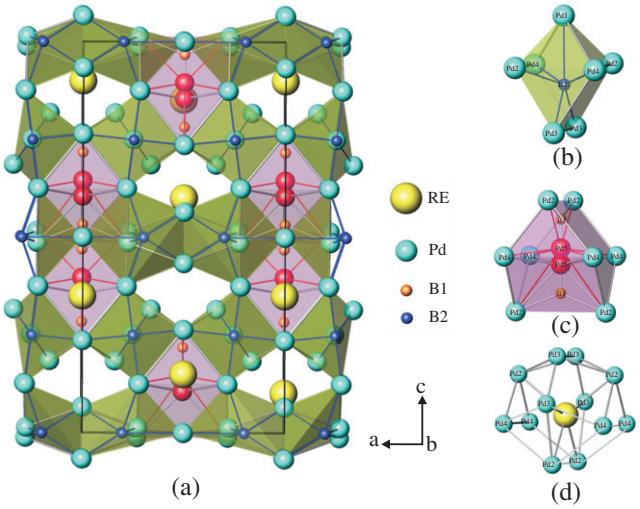

Figure 1. Crystal structure of $Nd_2Pd_{14+x}B_{5-y}$ in a three-dimensional view along the [010] axis (a) and coordination figures around B2 atoms (b), around B1–Pd5 atoms (c) and around Nd atoms (d).

2. Experimental details

Alloys with nominal composition $M_2Pd_{14}B_5$ and $M_2Pd_{15}B_5$, M = La, Ce, Pr, Nd, Sm, Eu, Gd, Lu as well as Th and U, with a weight of about 1 g each, were prepared by argon arc melting (weight loss less than 0.1%) on a water-cooled copper hearth in Ti-gettered argon from elemental ingots with minimal purity of 99.9 mass%. All alloys were sealed in quartz tubes under vacuum and annealed at 900 °C for 240 h before quenching in cold water. Single crystals were mechanically isolated from the crushed as-cast alloys $\{Nd, Th\}_2Pd_{14}B_5$. Inspection on an AXS-GADDS texture goniometer assured high crystal quality, unit cell dimensions and Laue symmetry of the specimens prior to x-ray intensity data collection on a four-circle Nonius Kappa diffractometer equipped with a CCD area detector. Orientation matrix and unit cell parameters for a tetragonal system were derived using the program DENZO [10]. No absorption corrections were necessary because of the rather regular crystal shape and small dimensions of the specimens investigated. The structures of $Nd_2Pd_{14+x}B_{5-y}$ and $Th_2Pd_{14+x}B_{5-y}$ were obtained by direct methods and refined with the aid of the SHELXL-97 program [11]. X-ray powder diffraction data from as-cast and annealed alloys were collected employing a Guinier–Huber image plate system with Cu Kα_1 ($8° < 2\theta < 100°$). Precise lattice parameters were calculated by least squares fits to the indexed 2θ values employing Ge as internal standard (a_{Ge} = 0.565 791 nm). Quantitative Rietveld refinement of x-ray powder diffraction data was performed with the FULLPROF program [12] using its internal tables for the atomic form factors. The as-cast and annealed samples were polished using standard procedures and were examined for single-phase condition by optical metallography and scanning electron microscopy (SEM). Compositions were determined via electron probe microanalyses (EPMA) on a Carl Zeiss DSM 962 equipped with a Link EDX system operated at 20 kV and 80 μA. The thorium–palladium–boride alloy was analyzed on a CAMECA SX50 wavelength dispersive spectrograph comparing the characteristic x-rays of the three elements in the alloy with those from the pure elements and standards (ThB_6 and Pd_2B) applying a peak deconvolution and ZAF correction procedure [13]. Measurements of the various physical properties were carried out on alloys $M_2Pd_{15}B_5$ with a series of standard techniques for which details can be obtained from [14].

3. Results and discussion

3.1. Crystal structure of $\{Nd, Th\}_2Pd_{14.9}B_{4.9}$

3.1.1. Crystal structure of $Nd_2Pd_{14.9}B_{4.9}$. Systematic extinctions, besides those for a body-centered unit cell, $(hk0)$ for $h = 2n + 1$ and $k = 2n + 1$, $(hh\ell)$ for $2h + \ell = 4n + 1$, (00ℓ) for $\ell = 4n + 1$, are compatible with the highest possible symmetry for the tetragonal space group type $I4_1/amd$. Determination of the atom arrangement in this space group type (origin at the center) was successful, employing direct methods suggesting one Nd and four Pd sites in the asymmetric unit. Two boron sites were located from a difference Fourier synthesis. This structure model was refined to a residual value $R_{F^2} = 0.12$ adopting anisotropic thermal displacement factors for the metal atoms but isotropic temperature factors for the borons, resulting in the chemical formula $Nd_2Pd_{15}B_5$. Standardization of the structure model with the program Structure Tidy [15] revealed at this stage a structure identical to the structure type of $Y_2Pd_{14}B_5$ [16].

Due to the rather high residual densities of $85e^-Å^{-3}$ left in $(0, \frac{1}{4}, 0.3989)$, the refinement at that stage was highly unsatisfactory. Therefore firstly occupancies of all metal sites were refined, but they did not reveal any significant deviations from full occupation. Inserting an additional Pd atom (Pd5) into the site $(0, \frac{1}{4}, 0.3989)$ reduced the residual density as well as the residual value to $R_{F^2} = 0.07$, however, at the expense of unacceptably high atom displacement parameters (ADPs) for Pd5 and unacceptably short distances among Pd5 atoms and between Pd5 and B1 atoms at the 4b site $(0, \frac{1}{4}, \frac{3}{8})$ (d_{B1-Pd5} = 0.0438 nm, $d_{Pd5-Pd5}$ = 0.0875 nm). Furthermore, the residual density of $24e^-$ Å^{-3} shifted to $(0, \frac{1}{4}, 0.4680)$. Relieving the occupancy of Pd5 to 45% and compensating the residual peak at $(0, \frac{1}{4}, 0.4680)$ by releasing the constraint on z_{B1} for the B1 atoms at an occupancy of ∼42% finally rendered normal ADPs for all atoms and reduced the total residual density below $2e^-Å^{-3}$.

As both the Pd5 as well as the B1 site, however, are only partially occupied (about 50% occupancy in each site), a complicated defect structure arises in which one Wyckoff position (either Pd5 or B1 exists) per unit cell is half-filled. It should be emphasized here that neither Pd5 atoms nor B1 atoms with z fixed at $(0, \frac{1}{4}, \frac{3}{8})$ supply a satisfactory solution ($R_{F^2} = 0.050$; residual densities $\geqslant 10e^-Å^{-3}$). It shall be furthermore noted that the final structure in all its detail is closely related to the $Sc_4Ni_{29}B_{10}$ type [17]. Results of the structure determination show a final value of R as low as 0.02, thus confirming the structure model, and are listed in table 1. The chemical formula turns out to be

Table 1. X-ray single-crystal data for $Nd_2Pd_{14.9}B_{4.9}$, and $Th_2Pd_{14.9}B_{4.9}$ (structure type related to $Sc_4Pd_{29}B_{10}$ type, space group $I4_1/amd$; No. 141) standardized with the program Structure Tidy [15]; standard deviations generally <0.0005 nm.

Parameter/compound	$Nd_2Pd_{15}B_5$	$Th_2Pd_{15}B_5$
Crystal size	$27 \times 54 \times 41$ μm^3	$50 \times 54 \times 90$ μm^3
a, c (nm)	$a = 0.857\,76(3)$, $c = 1.662\,78(4)$	$a = 0.861\,02(2)$, $c = 1.660\,19(5)$
ρ_x (Mg m^{-3}), μ_{abs}(mm^{-1})	9.95, 28.27	10.835, 43.90
Data collection Mo Kα, 2Θ range (deg)	$2 \leqslant 2\Theta \leqslant 72.6$	$2 \leqslant 2\Theta \leqslant 72.6$
Total number of frames	70 s/frame, 242 frames, 7 sets	50 s/frame, 222 frames, 7 sets
Reflections in refinement	$793 \geqslant 4\sigma(F_o)$ of 823	$763 \geqslant 4\sigma(F_o)$ of 827
Mosaicity	0.55	0.65
Number of variables	40	38
$R_{F^2} = \Sigma\lvert F_o^2 - F_c^2\rvert / \Sigma\lvert F_o^2\rvert$	0.020	0.026
$wR2$	0.058	0.062
R_{int}	0.062	0.069
GOF	1.227	1.081
Secondary extinction (Zachariasen)	0.000 43(1)	0.000 26(2)
	Atom parameters	
Nd or Th in 8e (0, $\frac{1}{4}$, z), z	0.100 22(3)	0.098 04(2)
Occ.	1.0	1.0
U_{11}, U_{22}, U_{33} (10^2(nm)^2)	0.0110(2), 0.0099(1), 0.062(2)	0.0128(2), 0.0099(1), 0.066(2)
Pd1 in 8d (0, 0, $\frac{1}{2}$)	—	—
Occ.	1.0	1.0
U_{11}, U_{22}, U_{33} (10^2(nm)^2)	0.0160(2), 0.0131(1), 0.107(2)	0.0168(3), 0.0149(3), 0.0130(3)
Pd2 in 16h (0, y, z), y, z	0.025 37(5), 0.236 40(3)	0.029 78(7), 0.237 06(3)
Occ.	1.0	1.0
U_{11}, U_{22}, U_{33} (10^2(nm)^2)	0.0139(2), 0.0086(2), 0.0084(2)	0.0203(2), 0.0104(2), 0.0093(2)
Pd3 in 16h (0, y, z), y, z	0.588 84(5), 0.065 85(2)	0.588 31(6), 0.066 05(3)
Occ.	1.0	1.0
U_{11}, U_{22}, U_{33} (10^2(nm)^2)	0.0098(2), 0.0078(2), 0.0053(2)	0.0148(2), 0.0094(2), 0.0064(2)
Pd4 in 16g (x, $x + \frac{1}{4}$, $\frac{7}{8}$), x	0.281 79(4)	0.284 09(5)
Occ.	1.0	1.0
U_{11}, U_{22}, U_{33} (10^2(nm)^2)	0.0130(2), 0.0119(2), 0.0096(3)	0.0221(2), 0.0135(2), 0.0110(3)
Pd5 in 8e (0, $\frac{1}{4}$, z), z	0.354 65(9)	0.373 94(9)
Occ.	0.45(1)	0.456(5)
U_{iso} (10^2(nm)^2)	0.0146(4)	0.036(2)
B1 in 8e (0, $\frac{1}{4}$, z), z	0.2827(15)	0.2851(35)
Occ.	0.43(1)	0.544(5)
U_{iso} (10^2(nm)^2)	0.017(6)	0.006(6)
B2 in 16f (x, 0, 0), x	0.1992(7)	0.2009(11)
Occ.	1.0	1.0
U_{iso} (10^2(nm)^2)	0.011(1)	0.016(1)
Residual density in e^- Å^{-3}, max, min	1.78, −2.10	4.12, −4.14

$Nd_2Pd_{14.9}B_{4.9}$. The crystal structure is presented in figure 1(a) in a three-dimensional view along the [010] axis. As one of the typical structural units for metal-rich borides, B2 atoms are found in deformed *triangular prisms* capped on one side by an additional Pd atom (figure 1(c)) whereas B1 atoms (defect site) are in a coordination unit formed by two trigonal prisms, face connected on a common quadratic base and formed by seven palladium atoms (figure 1(b)). Each rare earth atom is surrounded by six palladium atoms and six neighboring palladium atoms at a larger distance of 0.303 26 nm (figure 1(d)). Interatomic distances (table 1) generally agree well with the metallic radii of pure elements.

3.1.2. Crystal structure of $Th_2Pd_{14.9}B_{4.9}$. Determination of the crystal structure of $Th_2Pd_{14+x}B_{5-y}$ revealed essentially the same atom arrangement as found for $Nd_2Pd_{14.9}B_{4.9}$. Results of the structure determination show a final value of R as low as 0.026, thus confirming the structure model, and are listed in table 1. Whilst no indications were found for formation of an isostructural compound $U_2Pd_{14+x}B_{5-y}$, x-ray intensities and unit cell dimensions of the thorium analog compare well with the $Nd_2Pd_{14.9}B_{4.9}$ structure, implying structural analogy and suggesting similar sizes of Nd and Th atoms. The measured composition (from EPMA, in at.%), $Th_{9.3}Pd_{68.1}B_{22.5}$, is fully consistent with the formula $Th_2Pd_{14.9}B_{4.9}$ (in at.% $Th_{9.2}Pd_{68.3}B_{22.5}$).

Table 1. (Continued.)

Interatomic distances (nm); standard deviations generally <0.0005 nm					
Nd–2 Pd3	0.296 206	Pd3–2 B2	0.216 703	B1–2 Pd2	0.207 462
Nd–2 Pd2	0.297 252	Pd3–1 Pd3	0.266 790	B1–2 Pd1	0.221 185
Nd–2 Pd2	0.302 725	Pd3–2 Pd3	0.277 342	B1–1 Nd	0.303 256
Nd–4 Pd4	0.308 470	Pd3–2 Pd4	0.280 720		
Nd–2 Pd3	0.308 805	Pd3–2 Pd2	0.287 111		
		Pd3–1 Nd	0.296 206		
		Pd3–1 Nd	0.308 805		
Pd1–2 B1	0.221 185	Pd4–2 B2	0.221 304	B2–2 Pd3	0.216 703
Pd1–2 Pd5	0.276 157	Pd4–1 Pd5	0.266 853	B2–2 Pd4	0.221 304
Pd1–4 Pd4	0.281 028	Pd4–2 Pd3	0.280 720	B2–2 Pd2	0.225 343
Pd1–4 Pd2	0.289 181	Pd4–2 Pd1	0.281 028	B2–1 Pd1	0.258 100
Pd1–2 Nd	0.328 649	Pd4–2 Pd2	0.275 354	B2–1 Nd	0.303 256
		Pd4–2 Nd	0.308 470		
Pd2–1 B1	0.207 462	Pd5–4 Pd4	0.266 853		
Pd2–2 B2	0.225 343	Pd5–2 Pd2	0.275 354		
Pd2–1 Pd5	0.275 354	Pd5–2 Pd1	0.276 157		
Pd2–2 Pd3	0.287 111				
Pd2–2 Pd1	0.289 181				
Pd2–2 Pd4	0.297 012				
Pd2–1 Nd	0.297 252				
Pd2–1 Nd	0.302 725				

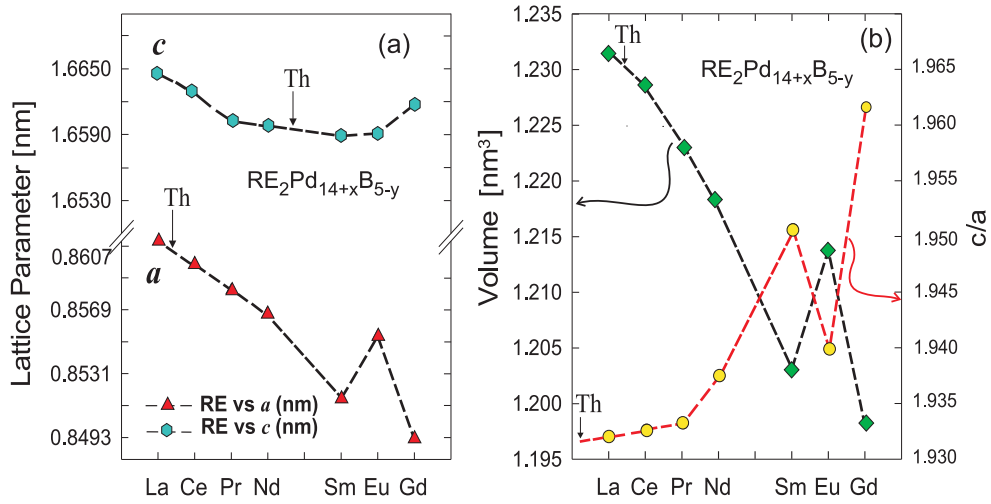

Figure 2. (a) Variation of the lattice parameters a and c versus rare earths in $M_2Pd_{14+x}B_{5-y}$. (b) Volume and c/a ratio of $M_2Pd_{14+x}B_{5-y}$. The positions of the lattice parameters of the Th compound are indicated by arrows.

3.2. Isotypic compounds $M_2Pd_{14+x}B_{5-y}$, M = La, Ce, Pr, Sm, Eu, Gd, Lu

Indexing of the x-ray powder patterns of $M_2Pd_{15}B_5$ alloys for M = Ce, Pr, Nd, Sm, Eu, Gd in all cases was complete and suggested a tetragonal unit cell close to that established for $Nd_2Pd_{14.9}B_{4.9}$. Analysis of the x-ray intensities, systematic extinctions, and size of unit cells suggest isotypism with the structure of $Nd_2Pd_{14.9}B_{4.9}$. Rietveld refinements with residual values generally below $R_F = 0.07$ confirmed the isotypism. A small but significant scatter in the lattice parameters (figure 2(a) and table 2) may indicate the existence of limited homogeneity regions. Figure 2(b), volume versus rare earth, indicates a 3+ ground state for Ce and Sm. The monotonic variation of both a and c parameters with rising ordinal number of the rare earths is consistent with a shrinking unit cell volume, i.e. the lanthanide contraction. The minor increase of the c/a ratio throughout the stability range of the $Nd_2Pd_{14.9}B_{4.9}$ structure type yields only a small increase of the lattice anisotropy. In contrast to the light rare earth analogs, the Eu-containing compound indicates a strong positive deviation from the unit cell volume variation versus the rare earths, i.e. a valence state close to the divalent Eu one.

A full profile Rietveld refinement performed on powder x-ray diffraction data for all alloys, however, cannot differentiate between slight differences in the occupancies of B1 and Pd5 atoms. Therefore for all RE homologs the structure model of $Nd_2Pd_{14.9}B_{4.9}$ was applied. The minor differences between the observed (Y_{obs}) and the calculated intensity (Y_{calc}) confirm the structure as well as the sample quality. A typical x-ray powder diffraction pattern and Rietveld refinement for $Ce_2Pd_{14+x}B_{5-y}$

Table 2. Lattice parameters and magnetic transition temperatures T_{mag}, effective magnetic moments μ_{eff} and paramagnetic Curie temperatures θ_p of $M_2Pd_{15}B_5$.

Compound	Lattice parameters a, c (nm)	T_{mag} (K)	μ_{eff}^{exp} (μ_B/RE)	μ_{eff}^{theo} (μ_B/RE^{3+})	θ_p
$La_2Pd_{15}B_5$	0.861 2(1), 1.664 3(3)				
$Ce_2Pd_{15}B_5$	0.859 1(4), 1.662 0(9)	0.5[a]	2.39	2.54	−2.29
$Pr_2Pd_{15}B_5$	0.858 2(2), 1.660 0(1)	0[a]	3.69	3.58	5.1
$Nd_2Pd_{15}B_5$	0.857 7(1), 1.662 8(1)	1[a]	3.58	3.62	−0.71
$Sm_2Pd_{15}B_5$	0.851 6(1), 1.658 9(4)	2[a]	0.92	0.84	2.5
$Eu_2Pd_{15}B_5$	0.856 2(7), 1.660 5(1)		5.4	7.94 for Eu^{2+}	−95
$Gd_2Pd_{15}B_5$	0.849 7(4), 1.661 4(8)	6.5	7.8	7.94	8
$Lu_2Pd_{15}B_5$	0.842 37(1), 1.658 24(4)				
$Th_2Pd_{15}B_5$	0.861 02(2), 1.660 19(5)				

[a] Extrapolated from Arrott plots and de Gennes scaling.

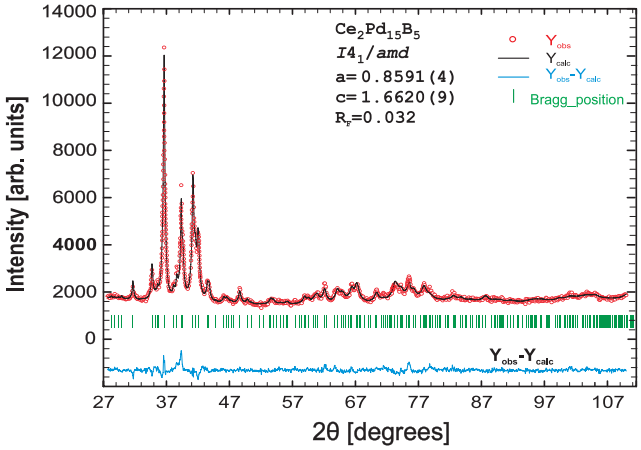

Figure 3. X-ray diffraction pattern of $Ce_2Pd_{14+x}B_{5-y}$. The solid line is the profile calculated from the Rietveld refinement. $Y_{obs} - Y_{calc}$ is the intensity difference between experimental data and Rietveld calculations.

is shown in figure 3. Attempts to synthesize the corresponding La-containing compound in single-phase condition failed, particularly due to the rather small temperature window of existence for this compound. Inspection by EMPA of an as-cast sample with nominal composition $La_2Pd_{14.9}B_{4.9}$ revealed a two-phase structure, which from Rietveld refinements confirmed the minor phase $La_2Pd_{14.9}B_{4.9}$ to comply with the tetragonal structure model of $Nd_2Pd_{14.9}B_{4.9}$ at a residual value of $R_F = 0.037$. On annealing, the tetragonal phase, however, disappears yielding a single main phase (also seen in the as-cast condition), which was indexed with a monoclinic x-ray powder spectrum. The detailed elucidation of the latter structure, $La_3Pd_{25-x}B_{8-y}$ ($x = 1.75$, $y = 0.07$; space group $P2_1/c$ with $a = 1.175\,67(2)$ nm, $b = 1.057\,57(2)$ nm, $c = 1.606\,64(3)$ nm, $\beta = 102.179(1)°$, $R_{F^2} = 0.03$), is the subject of a forthcoming paper [18]. In the absence of the La compound and in order to isolate the magnetic part of the physical properties we employed as an isotypic non-magnetic analog the newly discovered $Lu_2Pd_{14+x}B_{5-y}$ [19]. In section 3.3 we will use as a short form $M_2Pd_{15}B_5$ instead of $M_2Pd_{14+x}B_{5-y}$.

3.3. Bulk properties of $M_2Pd_{15}B_5$

Physical properties of $M_2Pd_{15}B_5$ (M = Ce, Pr, Nd, Sm, Eu, Gd, Lu) were investigated by means of temperature dependent specific heat, susceptibility/magnetization and resistivity measurements.

3.3.1. Specific heat. The experimental specific heat data $C_p(T)$ for $M_2Pd_{15}B_5$ are summarized in figure 4. $Lu_2Pd_{15}B_5$ is used as reference compound, representing the phonon contribution to $C_p(T)$. Within the low temperature limit ($T < 5$ K), the heat capacity of the latter can be accounted for by $C_p = \gamma T + \beta T^3$, yielding a Sommerfeld value $\gamma = 19$ mJ mol^{-1} K^{-2} and $\beta = 0.001\,77$ J mol^{-1} K^{-4}, revealing $\theta_D^{LT} = 289$ K.

A common procedure for approximating the overall heat capacity of metallic compounds usually assumes a Debye spectrum. In the present case, however, the simple Debye model did not yield convincing agreement with the experimental data, whereas adding three Einstein functions leads to accurate fitting results for the overall temperature range. In order to explore the vibrational properties in more detail, we subtracted the electronic contribution from the specific heat and adopted a model consisting of a combination of one Debye and three Einstein functions:

$$C_{ph}(T) = \frac{9R}{\omega_D^3}\int_0^{\omega_D}\frac{\omega^2(\frac{\omega}{2T})^2}{\sinh^2(\frac{\omega}{2T})}\,d\omega + \sum_{i=1,2,3} c_i R\,\frac{(\frac{\theta_{Ei}}{2T})^2}{\sinh^2(\frac{\theta_{Ei}}{2T})}. \quad (1)$$

Here, ω_D is the Debye temperature, $c_1 + c_2 + c_3 = 3n - 3$ is the number of optical branches of the dispersion relation and θ_{Ei} are the respective Einstein temperatures. The first part of equation (1) represents the standard Debye model and the second one accounts for three additional Einstein contributions. Thermal expansion of the solid, particularly at high temperatures, is not considered in equation (1). It should be noted that the Debye temperature ω_D according to equation (1) is determined only by the acoustic modes, whereas θ_D^{LT} evaluated from low temperature specific heat data ($C_p(T) = C_{el} + C_{ph} \equiv \gamma T + \beta T^3$ ($\theta_D = \sqrt[3]{(1944 \times n)/\beta}$)) is some value averaged over acoustic and optical branches of the

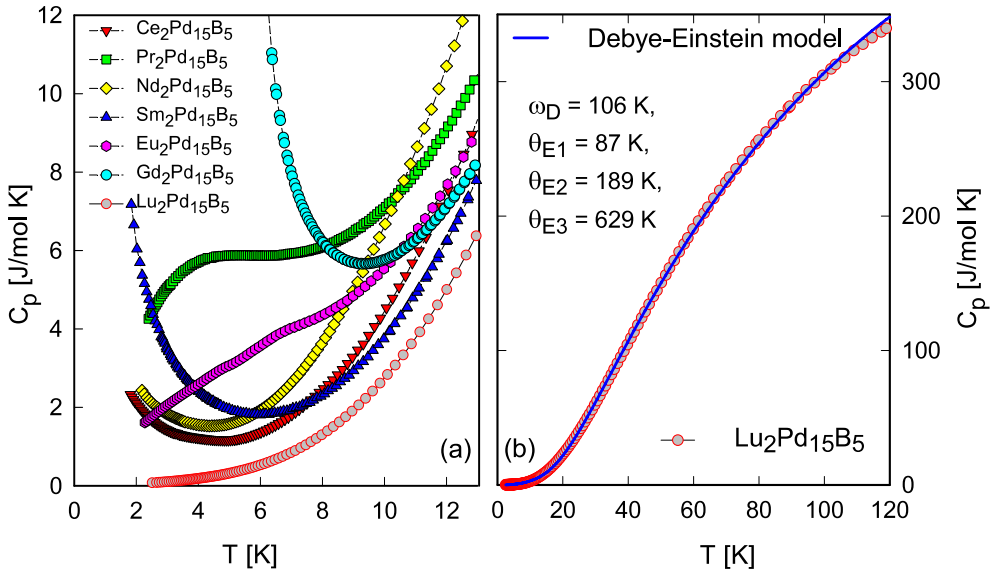

Figure 4. (a) Temperature dependent specific heat C_p of $M_2Pd_{15}B_5$ (M = Ce, Pr, Nd, Sm, Eu, Gd, Lu), plotted as C_p versus T. (b) C_p versus T for $Lu_2Pd_{15}B_5$. The solid line is a least squares fit according to equation (1).

phonon dispersion, contributing in a distinct manner to the low temperature specific heat.

Considering 22 atoms per formula unit, the phonon dispersion relation of $Lu_2Pd_{15}B_5$ consists of 3 acoustic and 63 optical branches. While the former constitute the Debye contribution, the latter form the Einstein part. In accordance with the compositional ratio among Lu, Pd and B, the weights are assumed to be $c_1 = 6$, $c_2 = 43$ and $c_3 = 14$ ($\sum c_i = 63$). Using these weights for the Einstein modes reveals a tentative fit of the experimental data (solid line in figure 4(b)) for a Debye temperature $\omega_D = 106$ K, Einstein temperatures $\theta_{E1} = 87$ K, $\theta_{E2} = 189$ K and $\theta_{E3} = 629$ K. To compare the Debye temperature deduced from the fit using equation (1) with the low temperature θ_D^{LT}, the former has to be multiplied with the factor $\sqrt[3]{n} = 2.8$, where $n = 22$ is the number of atoms per formula unit.

The heat capacities of the remaining materials investigated down to 2 K can be grouped into the compounds based on the following. (i) Gd, Sm, Nd, and Ce exhibit a rapid increase of $C_p(T)$ at low temperatures as a signature of the onset of long range magnetic order. Clearly, a mean-field type of transition in $Gd_2Pd_{15}B_5$ occurs at $T_{mag} = 6.5$ K (for more details see figure 6), while the $C_p(T)$ behavior of $Sm_2Pd_{15}B_5$ suggests ordering around 2 K. The upturn of $C_p(T)$ for both the Nd and the Ce based compounds indicates ordering at temperatures below 2 K (experimental limit). (ii) $Eu_2Pd_{15}B_5$ and $Pr_2Pd_{15}B_5$, on the other hand, do not show typical signs of ordering. The physics behind one observation, however, is different from that behind the other.

The absence of ordering in tetragonal $Pr_2Pd_{15}B_5$ is attributed to crystalline electric field (CEF) effects. CEF splitting of the $N = 2j + 1 = 9$-fold-degenerate ground state of the non-Kramers ion Pr^{3+} may result in singlets or non-magnetic doublet states, additionally to triplets or quartets. In the case where one of the former constitutes the ground state, a Pr compound does not show long range magnetic order. The non-magnetic state would manifest itself as a temperature independent susceptibility at low temperatures, as is obvious from the experimental results shown in figure 7. An estimation of the CEF influence can be obtained from an analysis of the magnetic contribution to the specific heat, C_{mag}. In a first approximation C_{mag} can be identified from the difference of the heat capacities of $Pr_2Pd_{15}B_5$ and non-magnetic $Lu_2Pd_{15}B_5$, i.e., $C_{mag} \approx \Delta C_p = C_p(Pr_2Pd_{15}B_5) - C_p(Lu_2Pd_{15}B_5)$. The data for the latter are corrected with respect to the large mass difference between Pr and Lu. $C_{mag}(T)$ for $Pr_2Pd_{15}B_5$ is characterized by two broad maxima centered around 6 K and 60 K, respectively. Integrating $C_{mag}(T)/T$ yields the magnetic entropy, S_{mag}, shown as a dashed–dotted line in figure 5. A plateau-like structure between 10 and 20 K is in line with $S_{mag} = 2R \ln 2$, while at the highest temperatures $2R \ln 9$ is reached. Note that two rare earth ions in the unit cell double the entropy values. Releasing an entropy value of $R \ln 2$ in the absence of long range magnetic order or, e.g., a Kondo effect, can be associated with singlets as the ground state and as the first excited level. To account for all of the $C_{mag}(T)$ data, a Schottky curve was adjusted to the experimental data (see the dashed and the solid lines in figure 5(a)), revealing fair agreement for the first excited level at 10 K (dashed line); a quasi-quartet state is situated around 160 K, followed by a doublet at 220 K and an uppermost singlet around 400 K. A second attempt to better render the low temperature maximum in $C_{mag}(T)$ was made assuming the first excited level at 15 K (solid line). Obviously, neither of these basic approaches fully accounts for the experimental findings, most likely because of a large dispersion of the first excited CEF level due to magnetic exchange interactions. The latter was evidenced from inelastic neutron scattering experiments, e.g., in the case of tetragonal $PrNi_2B_2C$ [20].

The absence of long range magnetic order in $Eu_2Pd_{15}B_5$ is a consequence of a non-magnetic ground state of the Eu ions. Eu, in general, may adopt either the non-magnetic Eu^{3+} or

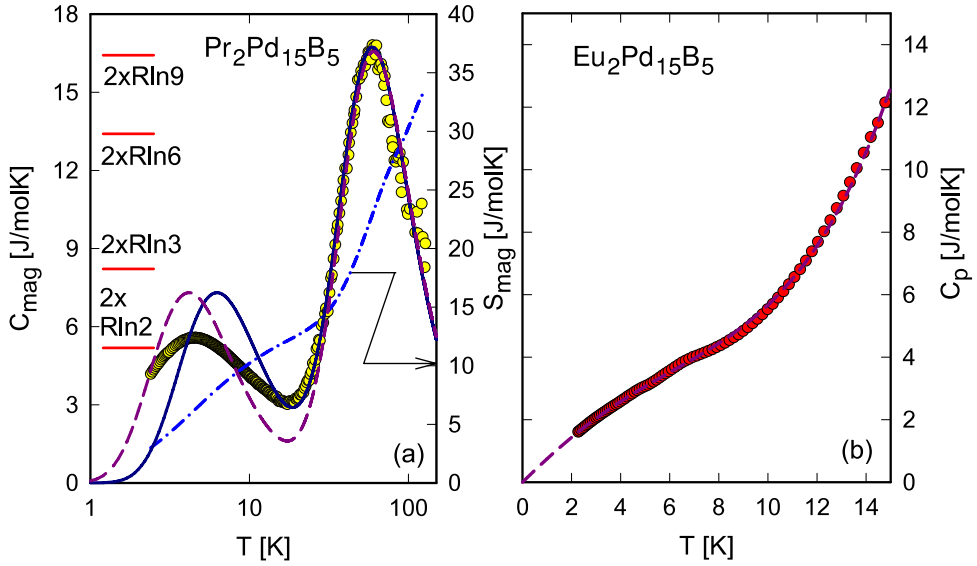

Figure 5. (a) Magnetic contribution to the specific heat, C_{mag}, of $Pr_2Pd_{15}B_5$. The solid and the dashed lines are fits in terms of the Schottky contribution. The dashed–dotted line represents the magnetic entropy of $Pr_2Pd_{15}B_5$ and refers to the right axis. (b) Low temperature specific heat of $Eu_2Pd_{15}B_5$; the dashed line is a least squares fit according to the spin fluctuation model, equation (2).

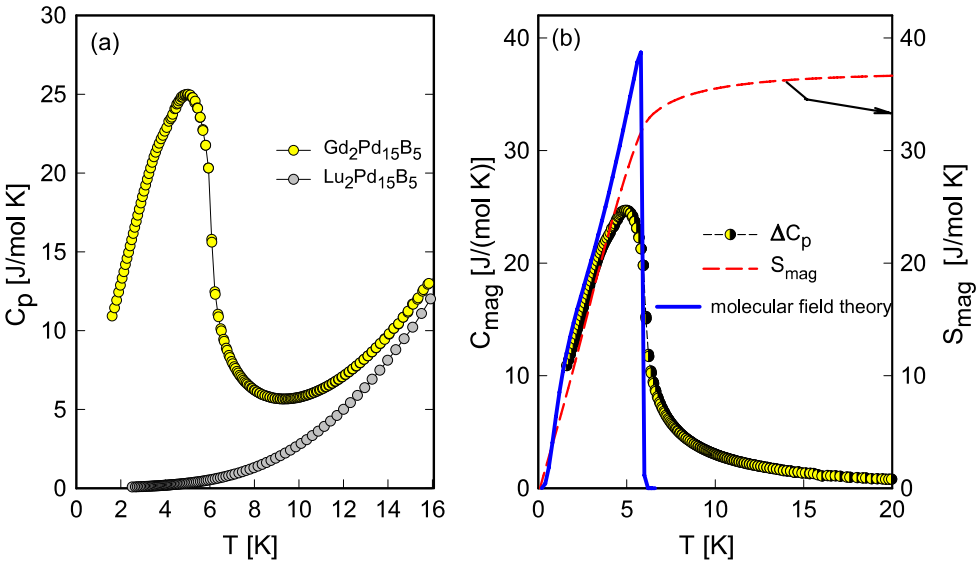

Figure 6. (a) Temperature dependent specific heat, C_p, of $Gd_2Pd_{15}B_5$ and $Lu_2Pd_{15}B_5$. (b) Magnetic contribution to the specific heat, C_{mag}, of $Gd_2Pd_{15}B_5$. The solid line constitutes the heat capacity of in the scope of the molecular field model with $j = 7/2$ and $T_{\mathrm{C}} = 6.5$ K. The dashed line represents the magnetic entropy of $Gd_2Pd_{15}B_5$ and refers to the right axis.

the magnetic Eu^{2+} state. In a dynamic scenario, intermediate states are possible, resulting from fluctuations with typical time constants between the 2+ and the 3+ state. The lattice parameters observed (compare figure 2(a)) obviously refer to a substantial variance of the Eu ion from the 3+ state with an electronic configuration EC = $4f^6$. The proximity of the EC of Eu to the magnetic $4f^7$ state, however, cannot be derived from the lattice parameters only. In the hypothetical case that Eu adopts the 2+ state (EC = $4f^7$), a behavior akin to that of $Gd_2Pd_{15}B_5$ would be expected, i.e., magnetic ordering around 6 K. Such a resemblance is an outcome of the identical EC of Eu^{2+} and Gd^{3+} resulting in the same de Gennes factor $dG \propto T_{\mathrm{mag}}$. In the context of the lattice parameters deduced and the observation that, most probably, $Eu_2Pd_{15}B_5$ does not exhibit long range magnetic order, an intermediate valence state of the Eu ions in $Eu_2Pd_{15}B_5$ is conceivable. In fact, the effective moment derived ($\mu_{\mathrm{eff}} = 5.91\ \mu_{\mathrm{B}}$) is well below the moment expected for a $j = 7/2$ state (compare figure 7). A static picture of a mixed valence state is not likely since the crystalline unit cell contains only one equivalent rare earth site, i.e., the 8e site. Minor specific heat anomalies at 4 and 6 K (visible kinks in figure 5(b)) may be due to $EuPd_3B$ and Eu_3O_4 impurities, respectively. These phases exhibit magnetic ordering at these temperatures [21, 22]. Traces of $EuPd_3B$ are seen in EPMA analyses.

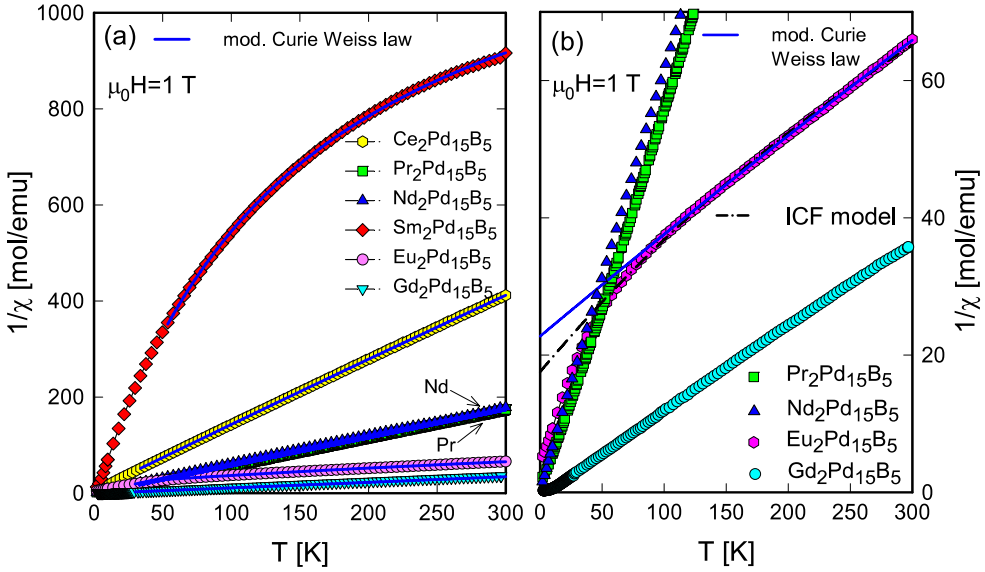

Figure 7. (a) Temperature dependent magnetic susceptibility χ of $M_2Pd_{15}B_5$ plotted as $1/\chi$ versus T in a magnetic field 1 T. M = Ce, Pr, Nd, Sm, Eu and Gd (b) $1/\chi$ versus T for $M_2Pd_{15}B_5$, M = Pr, Nd, Eu, and Gd. The solid lines in (a) and (b) represent the modified Curie–Weiss law and the dashed–dotted line is a least squares fit according to the ICF model.

An analysis of the low temperature $C_p(T)$ data can be done when assuming that valence fluctuations between the 2+ and the 3+ state come along with spin fluctuations between the $4f^6$ and the $4f^7$ EC. One of the archetypal systems studied with respect to spin fluctuations is UAl_2, where the heat capacity at low temperatures was successfully accounted for by [23]

$$C_p = \gamma T + \beta T^3 + \delta \ln \frac{T}{T^*} \tag{2}$$

where both former terms are the standard expressions for simple metals and the latter represents the contribution due to spin fluctuations. The absorption and re-emission of spin fluctuations renormalizes the electronic self-energy, leading to an enhanced effective mass at low temperatures [24]. As a consequence, the electronic specific heat coefficient γ is enhanced as well.

A least squares fit of the heat capacity data of $Eu_2Pd_{15}B_5$ is shown in figure 5 as a dashed line. The parameters deduced reveal a remarkably large value of γ ($\gamma \approx 0.38$ J mol^{-1} K^{-2} for Eu) and a spin fluctuation temperature $T^* \approx 50$ K. A spin fluctuation scenario seems to be justified from the fact that the intermediate valence due to valence fluctuations between the 2+ and the 3+ state drives fluctuations of the magnetic state from $4f^7$ to $4f^6$.

The magnetic phase transition of $Gd_2Pd_{15}B_5$ is shown in more detail in figures 6(a) and (b) in conjunction with non-magnetic $Lu_2Pd_{15}B_5$. The anomaly due to the magnetic phase transition at $T_C = 6.5$ K of $Gd_2Pd_{15}B_5$ shows up as a rounded, mean-field-like jump. When idealizing the rounded anomaly to a sharp jump, its approximate magnitude is reproduced in terms of the molecular field model. In terms of this model, the molecular field parameter Γ follows from $\Gamma = [(3 \times 0.266)/(j(j+1)g_j^2)]T_c$, if only next nearest neighbor interaction is considered. For $j = 7/2$ and the Landé factor $g_j = 2$, $\Gamma = 0.082$ for $T_c = 6.5$ K. This parameter without any other adjustable factors yields the heat capacity curve shown as a solid line in figure 6(b). Note that the jump of C_{mag} at $T = T_c$ is derived in the molecular field model as

$$\Delta C_{mag}(T = T_c) = 5R\frac{j(j+1)}{2j^2+2j+1}. \tag{3}$$

Considering the fact that the molecular field model does not account for any short range correlations which in the case of $Gd_2Pd_{15}B_5$ transfer about 10% of the entropy gain to temperatures above T_C (see below) and thus reduce C_{mag} below T_C, the theoretical mean-field value $\Delta C_{mag} = 2 \times 20.15$ J mol^{-1} K^{-1} for $j = 7/2$ systems agrees reasonably well with the experimental data. The magnetic entropy gain is calculated from the area below C_{mag}/T and is shown as a dashed line in figure 6(b). Taking into account the two Gd ions per formula unit yields $S_{mag} = 2 \times R\ln(2j+1) = 34.57$ J mol^{-1} K^{-1} at $T = T_C$, which has to be compared with the experimental result of 33.5 J mol^{-1} K^{-1} at T_C. Since Gd systems do not suffer CEF effects, no further magnetic contributions should occur above T_C. The slight increase of S_{mag} for $T > T_C$ is attributed to the non-vanishing $C_{mag}(T)$ due to short range order effects above T_C, and possibly modified by non-coinciding phonon spectra of both the Gd and Lu based compounds.

3.3.2. Magnetism. $\chi(T)$ measurements were performed in 0.1, 1 and 3 T and show a good scaling indicating that there are no magnetic impurities except for Eu. In this case a small hump occurs in low fields (<0.1 T) at about 6 K which is however suppressed for fields larger than 0.1 T. Figure 7 shows the temperature dependent magnetic susceptibility χ plotted as $1/\chi$ versus T for $M_2Pd_{15}B_5$, M = Ce, Pr, Nd, Sm, Eu, Gd in a magnetic field of 1 T. Common to all the compounds investigated is a Curie–Weiss-like behavior at

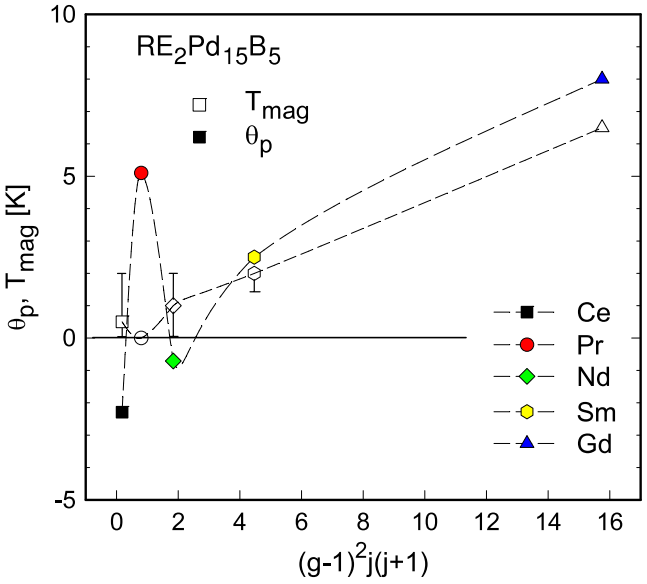

Figure 8. The de Gennes scaling of the paramagnetic Curie temperature θ_p and the magnetic phase transition temperature T_{mag}. The empty and filled symbols refer to T_{mag} and θ_p, respectively.

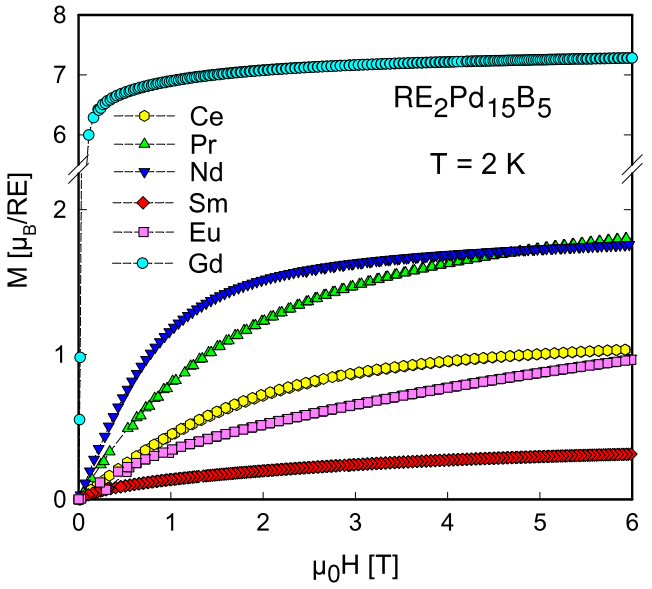

Figure 9. Isothermal magnetization M versus $\mu_0 H$ of $M_2Pd_{15}B_5$ at 2 K. The inset shows data on an expanded magnetization scale.

elevated temperatures, except for $Sm_2Pd_{15}B_5$ which exhibits a rather curved $1/\chi$ dependence due to the closely spaced $j = 5/2$ and $7/2$ Hund's multiplets, a feature occurring in many Sm based intermetallics. A similar situation is met for $Eu_2Pd_{15}B_5$ (see below).

To qualitatively account for the region above about 50 K, least squares fits according to the modified Curie–Weiss law, i.e., $\chi = \chi_0 + C/(T - \theta_p)$, were applied. χ_0 represents a temperature independent Pauli-like susceptibility, C is the Curie constant and θ_p is the paramagnetic Curie temperature. Results from this procedure are summarized in table 2. Almost all effective magnetic moments μ_{eff} of this series are very near to the theoretical values associated with the 3+ state of the particular rare earth ion, thereby indicating rather stable magnetic moments.

The exception as regards μ_{eff} concerns $Eu_2Pd_{15}B_5$, where $\mu_{eff} = 5.4\ \mu_B$ is below the value expected for a total angular momentum $j = 7/2$ ($\mu_{eff} = 7.94\ \mu_B$). In order to receive information about the dynamics of the intermediate state, the magnetic susceptibility was further interpreted in terms of the *interconfiguration fluctuation model*, ICF [25]. Indeed, a least squares fit reveals the magnetic $4f^7$ EC as the ground state separated by an excitation energy E_{ex} in the order of several tenths of a kelvin and a spin fluctuation temperature $T_{sf} \approx 70$ K (compare the dashed–dotted line in figure 7(b)). The almost degenerate states $4f^7$ and $4f^6$ provide then a natural explanation for the intermediate valence in $Eu_2Pd_{15}B_5$. T_{sf} derived from the susceptibility data is of the same magnitude as T^* obtained in terms of equation (2).

The paramagnetic Curie temperatures θ_p derived show positive as well as negative values (compare figure 8). While θ_ps are negative for the early RE elements Ce and Nd, θ_ps are positive for the systems based on Sm and Gd. $Pr_2Pd_{15}B_5$ is characterized by a positive paramagnetic Curie temperature. In general, negative values are indicative of antiferromagnetic interactions between magnetic ions; positive values, in contrast, are characteristics of ferromagnetic interplay, accompanied by ferromagnetic ordering. A change of the type of interaction among a series of rare earth intermetallics has recently been found, e.g., in $REPt_3Si$ [3] and is supposed to be a consequence of the distant dependent RKKY (Rudermann, Kittel, Kasuya, and Yosida) interaction, driven by the shrinking unit cell dimensions from Ce to Gd due to the regular lanthanoid contraction.

To obtain information about the type of ordering as well as of the CEF ground state, isothermal magnetization measurements were performed. Results from the 2 K runs are displayed in figure 9. Except for $Gd_2Pd_{15}B_5$, the $M(H)$ curves, in agreement with the heat capacity data, do not evidence signs of long range magnetic order above 2 K. Additionally, the magnetization data observed at 6 T are well below the respective $g_j j$ values, as a consequence of the lifting of the $2j+1$-fold-degenerate ground state by crystalline field effects. Since for Gd and Eu systems only spin contributions add to the total angular momentum, no CEF effects are expected to occur.

Comparing $M(H)$ for $Pr_2Pd_{15}B_5$ and $Nd_2Pd_{15}B_5$ shows that in the low field limit the magnetization of the Pr system is well below that of the Nd one. This can be interpreted using the fact that the ground state of the Pr system is non-magnetic. On the other hand, in the 6 T limit the two compounds have about the same magnetization as a consequence of the almost equal values of $M_{RE} = g_j j$. An important observation can be made when comparing $M(H)$ data for $Gd_2Pd_{15}B_5$ and $Eu_2Pd_{15}B_5$. As already obvious from the absence of long range magnetic order, a magnetic 2+ state is not realized for the Eu ion in $Eu_2Pd_{15}B_5$. This is also manifested from the significant difference of the $M(H)$ data derived at 6 T: while the Gd compound approaches the saturation magnetization (7 μ_B), the Eu based compound reaches 1 μ_B. A simple linear interpolation would then locate the Eu valence around 2.85.

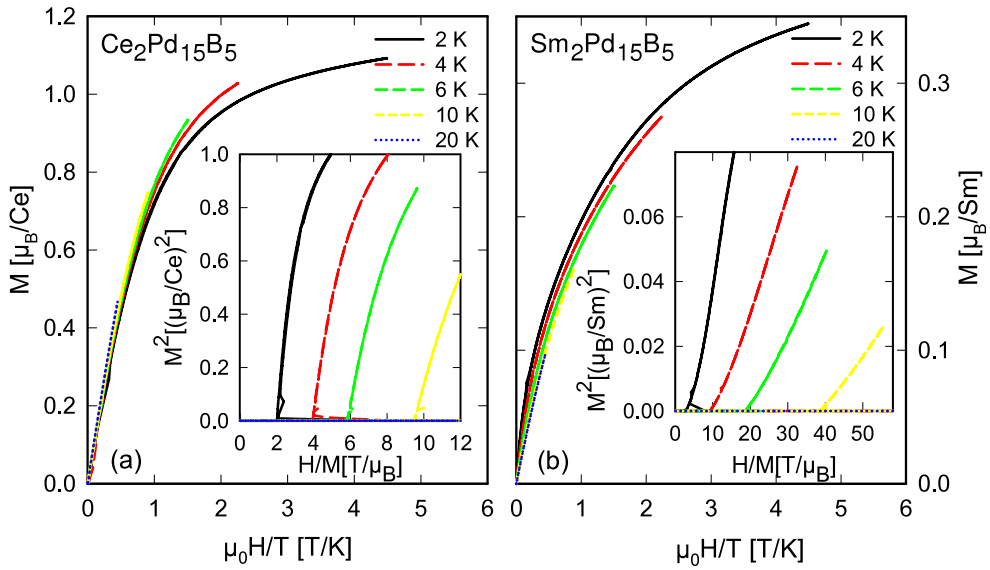

Figure 10. (a) Magnetization M of $Ce_2Pd_{15}B_5$ plotted as M versus $\mu_0 H/T$. The inset shows the Arrott plot. (a) Magnetization M of $Sm_2Pd_{15}B_5$ plotted as M versus $\mu_0 H/T$. The inset displays the Arrott plot.

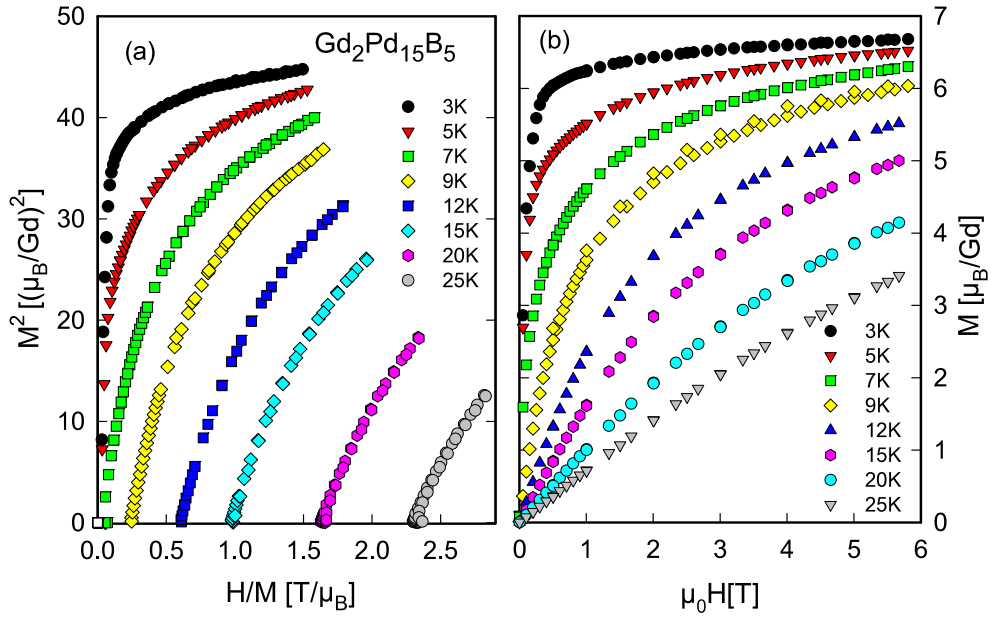

Figure 11. (a) Arrott plot of $Gd_2Pd_{15}B_5$. (b) Magnetization M of $Gd_2Pd_{15}B_5$ plotted as M versus $\mu_0 H/T$.

The small magnetization observed for $Sm_2Pd_{15}B_5$ is in line with the small value of $g_j j = 0.84\ \mu_B$.

Arrott plots (shown as examples for the Ce and the Sm based compounds in the insets of figures 10(a) and (b)) corroborate the conclusions drawn from specific heat measurements. While extrapolations to $T = 0$ for M^2 versus H/M for $Ce_2Pd_{15}B_5$, $Nd_2Pd_{15}B_5$ and $Sm_2Pd_{15}B_5$ make long range magnetic order rather likely, the same procedure is not indicative of ordering at finite temperatures in the case of $Pr_2Pd_{15}B_5$ and $Eu_2Pd_{15}B_5$. On the contrary, Arrott plots evidence the ferromagnetic phase transition at $T = 6.5$ K for $Gd_2Pd_{15}B_5$ (figure 11(a)). Although the transition temperatures, except in the case of $Gd_2Pd_{15}B_5$, could not be accessed through magnetic measurements, the behavior of the magnetization curves right above T_{mag} gives strong indications about the type of ordering: plotting the data as M versus $\mu_0 H/T$ reveals for typical antiferromagnetic systems a shift of the data sets from right to left if the temperatures increase as a result of the negative molecular field constant; the opposite occurs for ferromagnets. Indeed, the present magnetization curves (figures 10(a) and (b)) are indicative of antiferromagnetic order in $\{Ce, Nd\}_2Pd_{15}B_5$ but evidence ferromagnetism for $\{Sm, Gd\}_2Pd_{15}B_5$.

3.3.3. Electrical resistivity. The temperature dependent electrical resistivity $\rho(T)$ of $M_2Pd_{15}B_5$, M = Ce, Pr, Nd,

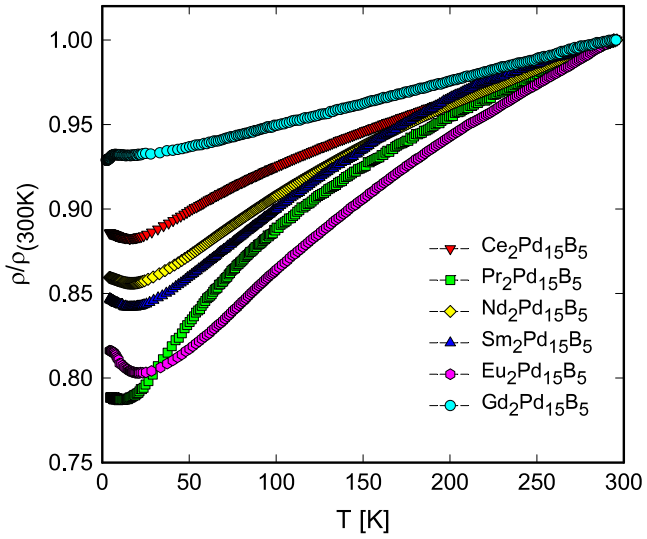

Figure 12. Temperature dependent electrical resistivity ρ of $M_2Pd_{15}B_5$ plotted in a normalized representation. M = Ce, Pr, Nd, Sm, Eu, Gd, Lu.

Sm, Eu, Gd and Lu, is shown in figure 12 in a normalized representation for temperatures above 4.2 K. The electrical resistivity, ρ, of $M_2Pd_{15}B_5$ is, in general, characterized by small RRR values primarily caused by defects inherent to the present crystal structure.

The low temperature resistivity behavior is distinguished by a minimum in $\rho(T)$ in the vicinity of 20 K followed by an increase towards lower temperatures. A non-magnetic-origin-like variable range hopping is conceivable due to statistical disorder of atoms within the crystal structure, as well as a magnetic origin from superzone boundary effects above a magnetic phase transition or from short range order effects above T_{mag}. At first sight, magnetic correlations as the origin seem more likely, since magnetic fields of the order of several teslas completely suppress the anomalies indicated above.

Details of the low temperature resistivity are shown for M = Ce, Pr, Eu and Gd in figure 13. Obviously, the application of external magnetic fields causes a suppression of the anomalies associated with long range magnetic order in the case of Ce and Gd, as well as the anomalies linked to the non-magnetic ground state of the Pr and the Eu system. The change of the resistivity upon the application of magnetic fields is extremely small. The only exception found in the whole series is for $Eu_2Pd_{15}B_5$, where the application of 12 T at $T = 2$ K changes the resistivity by about 10%. A rapid decrease of the resistivity in the case of $Gd_2Pd_{15}B_5$ below the maximum at about 6 K results from the onset of long range magnetic order and is in agreement with magnetization and heat capacity measurements.

The fact that the Lu based compound as well as the systems having non-magnetic ground states, i.e., Pr and Nd, would be equally likely suggests a non-magnetic origin of the resistivity increase observed towards low temperatures. A proof of this proposition in terms of Mott's variable range hopping mechanism [26] is difficult because of the extremely small changes of the absolute resistivity values of these compounds and, thus, least squares fits are rather unreliable.

4. Summary

The crystal structure of novel ternary compounds $M_2Pd_{14+x}B_{5-y}$ (M = La, Ce, Pr, Nd, Sm, Eu, Gd and Th) was

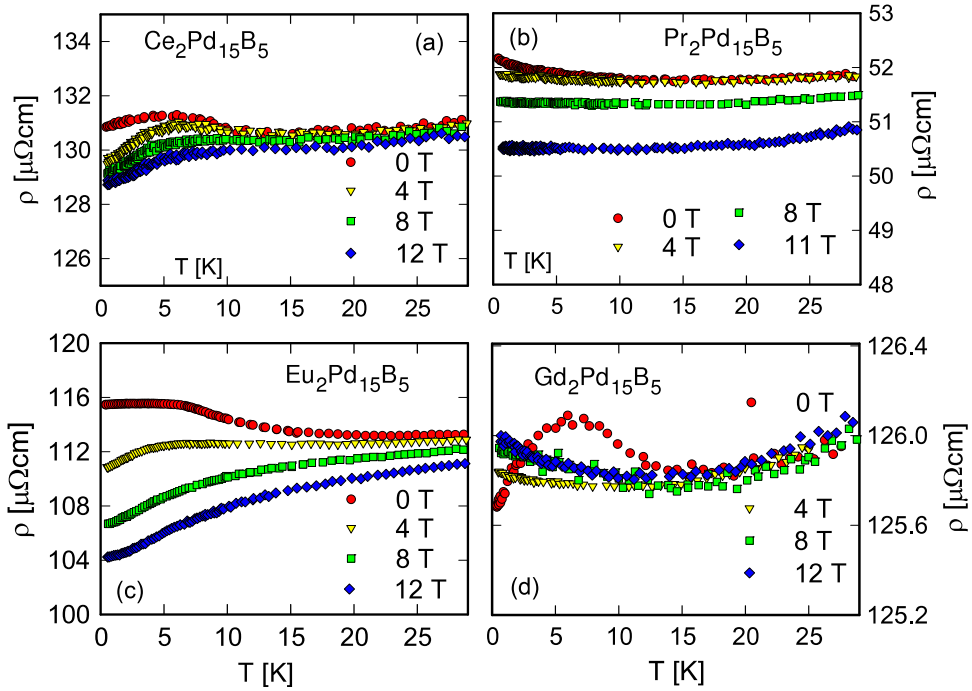

Figure 13. Low temperature resistivity $\rho(T)$ of $M_2Pd_{15}B_5$ for various values of applied external fields. (a) M = Ce; (b) M = Pr; (c) M = Eu; (d) M = Gd.

determined from x-ray single-crystal data for $Nd_2Pd_{15}B_5$ and $Th_2Pd_{15}B_5$ and was found to be closely related to the structure type of $Sc_4Ni_{29}B_{10}$ with tetragonal unit cell and space group type $I4_1/amd$. All rare earth homologs were characterized by Rietveld analyses to be isotypic with the $Nd_2Pd_{15}B_5$ type.

Physical properties are primarily determined by two effects: (i) the magnetic moment of the respective rare earth ion and associated CEF effects; (ii) intrinsic defects of the crystal structure. The latter is clearly responsible for the rather small RRR values ($RRR_{min} = 1.07$ for Gd and $RRR_{max} = 1.26$ for Pr based compounds) deduced from electrical resistivity measurements. The former, of course, determines the magnetic ground state. Clear evidence for long range magnetic order is found for $Gd_2Pd_{15}B_5$, while solid indications of magnetic ordering are found for the Ce, Nd and Sm systems. The shrinking unit cell volume, when proceeding from $Ce_2Pd_{15}B_5$ to $Gd_2Pd_{15}B_5$, modifies the RKKY interaction such that antiferromagnetic interactions ($\theta_p < 0$) gradually change to ferromagnetic ones ($\theta_p > 0$) and as a consequence, $Gd_2Pd_{15}B_5$ orders ferromagnetically at $T_C = 6.5$ K. Due to CEF effects, $Pr_2Pd_{15}B_5$ is non-magnetic at low temperatures, while $Eu_2Pd_{15}B_5$ is dominated by spin fluctuations driven by the intermediate valence state of the Eu ion.

Acknowledgments

This research was supported by the Austrian National Science Foundation FWF project P18054-Phy. PR and OS are grateful for short term missions within the action COST P16 at ITN/Sacavem and University Vienna, respectively.

References

[1] Bauer E, Hilscher G, Michor H, Paul C, Scheidt E-W, Gribanov A, Seropegin Y, Noël H, Sigrist M and Rogl P 2004 *Phys. Rev. Lett.* **92** 027003
[2] Yogi M, Kitaoka K, Hashimoto S, Yasuda T, Settai R, Matsuda T D, Haga Y, Onuki Y, Rogl P and Bauer E 2004 *Phys. Rev. Lett.* **93** 027003
[3] Bauer E, Lackner R, Hilscher G, Michor H, Sieberer M, Eichler A, Gribanov A, Seropegin Y and Rogl P 2005 *J. Phys.: Condens. Matter* **17** 1877
[4] Yogi M, Mukuda H, Kitaoka Y, Hashimoto S, Yasuda T, Settai R, Matsuda T D, Haga Y, Onuki Y, Rogl P and Bauer E 2006 *J. Phys. Soc. Japan* **75** 013709
[5] Bauer E, Kaldarar H, Prokofiev A, Royanian E, Amato A, Seren J, Brämer-Escamilla W and Bonalde I 2007 *J. Phys. Soc. Japan* **76** 051009
[6] Kimura N, Ito K, Saitoh K, Umeda Y, Aoki H and Terashima T 2005 *Phys. Rev. Lett.* **95** 247004
[7] Malik S K, Dhar S K and Vijayaraghavan R 1984 *Bull. Mater. Sci.* **6** 263
[8] Lackner R, Bauer E and Rogl P 2006 *Physica* B **378–380** 835
[9] Loison C, Leithe-Jasper A and Rosner H 2007 *Phys. Rev.* B **75** 205135
[10] Nonius *Kappa CCD Program Package COLLECT, DENZO, SCALEPACK, SORTAV* Nonius, Delft, Netherlands
[11] Sheldrick G M 1997 *SHELXL-97, Program for Crystal Structure Refinement* University of Göttingen, Germany, Windows version by McArdle, Natl. Univ. Ireland, Galway
[12] Roisnel T and Rodriguez-Carvajal J 2001 *Mater. Sci. Forum* **378–381** 118
[13] Pouchou J L and Pichoir F 1985 *J. Microsc. Spectrosc. Electron.* **10** 279
[14] Bauer E, Berger St, Paul Ch, Della Mea M, Hilscher G, Michor H, Reissner M, Steiner W, Grytsiv A, Rogl P and Scheidt E-W 2002 *Phys. Rev.* B **66** 214421
[15] Parthé E, Gelato L, Chabot B, Penzo M, Cenzual K and Gladyshevskii R 1994 *TYPIX-Standardized Data and Crystal Chemical Characterization of Inorganic Structure Types* (Berlin: Springer)
[16] Salamakha P, Goncalves A P, Sologub O and Almeida M 2003 *J. Alloys Compounds* **360** 61
[17] Kuz'ma Y B, Dub O M, Bruskov V A, Chaban N and Zavalii L V 1988 *Kristallografiya* **33** 841
[18] Sologub O, Rogl P, Grytsiv A and Giester G 2009 *J. Phys.: Conf. Ser.* submitted
[19] Sologub O, Rogl P and Giester G 2009 in preparation
[20] Mazumdar C, Rotter M, Frontzek M, Michor H, Doerr M, Kreyssig A, Koza M, Hiess A, Voigt J, Behr G, Gupta L C, Prager M and Loewnhaupt M 2008 *Phys. Rev.* B **78** 144422
[21] Dhar S K, Nagarajan R, Malik S K and Vijayaraghavan R 1984 *Phys. Rev.* B **29** 5953
[22] Batlogg B, Kaldis E, Schlegel A and Wachter P 1975 *Phys. Rev.* B **12** 3940
[23] Trainor R J, Brodsky M B and Culbert H V 1975 *Phys. Rev. Lett.* **34** 1019
[24] Doniach S and Engelsberg S 1966 *Phys. Rev. Lett.* **17** 750
[25] Sales B C and Wohlleben D K 1975 *Phys. Rev. Lett.* **35** 1240
[26] Mott N 1970 *Phil. Mag.* **22** 7